RESEARCH PAPER

Third Order Nonlinear Optical, Electrochemical, Catalytic, and Antibacterial Properties of Green Synthesized $BaSnO_3$ Nanoparticles

Suganya Murugesan[1], Kayathiri Chembian[1], Balu Rajavelu[1,*], Vinitha Gandhiraj[2], Zion Delci[3], Chitra Devi Saravanan[1], Devendran Kaliyamoorthy[1], Sriramraj Mathiyalagan[1]

* *arbalu757@gmail.com*

[1] PG and Research Department of Physics, AVVM Sri Pushpam College (Affiliated to Bharathidasan University, Tiruchirappalli), Poondi, Tamilnadu, India
[2] School of Advanced Science, Vellore Institute of Technology, Chennai, Tamilnadu, India
[3] PG Department of Physics, Dwaraka Doss Goverdhan Doss Vaishnav College, Chennai, Tamilnadu, India

Received: August 2022 **Revised: November 2024** **Accepted: Drcember 2024**
DOI: 10.22068/ijmse.2966

Abstract: *Perovskite materials are widely studied for their super-conducting, magnetic, catalytic, and electro-optic properties. Among them, barium stannate ($BaSnO_3$) finds applications in dielectric and optically active devices, thermally stable capacitors, and humidity and gas sensors. This research compared the electrochemical, third-order nonlinear, dye-deactivation, and bacterial growth inhibition capabilities of $BaSnO_3$ produced by chemical (CBS) and greener (GBS) methods. The decreased crystallite size was realized for the green synthesized $BaSnO_3$. Energy band gaps were 3.23 and 3.04 eV for CBS and GBS, respectively. The GBS sample exhibited increased specific capacitance value. Photocatalytic degradation efficiencies were 78.4% and 89.7%, respectively for $BaSnO_3$ synthesized by normal and greener approach against methyl violet after 90 min of UV light irradiation. Enhanced nonlinear optical parameters were obtained for the GBS sample. Excellent antibacterial efficacy against Proteus vulgaris bacteria was realized for GBS thanks to the domination of phytochemicals of M. olifera leaf extract.*

Keywords: *$BaSnO_3$ perovskite, Bacteria suppression, Green synthesis, Specific capacitance.*

1. INTRODUCTION

Perovskite materials with super-conducting, magnetic, and electro-optic properties [1] find applications as catalysts, proton and oxygen-ionic conductors, electrochemical and magnetic devices, etc. [2]. Amongst the perovskite materials, earth alkaline stannate with chemical formula $MSnO_3$ (M= Ba, Sr, and Ca) which forms a component of dielectric materials used in thermally stable capacitors, photoelectron-chemical energy conversion, gas sensors, etc. [3]. Barium stannate ($BaSnO_3$), being stable up to 1000°C exhibits n-type conductivity with a band gap of 3.4 eV which makes it suitable for applications in dielectric devices, thermally stable capacitors, humidity and gas sensors, optical applications, ceramic boundary layers, etc. [4, 5]. However, the insulating behaviour of $BaSnO_3$ at room temperature limits its viability for various technological applications. To utilize $BaSnO_3$ for optoelectronic, catalytic, magnetic, and bio-medical applications, its band gap must be lowered which is achievable through doping with impurities. James et al. [1] observed improved optical and magnetic properties for Fe-doped $BaSnO_3$ nanopowders. An electrical resistivity of 2.43 Ω-cm has been realized for $BaSnO_3$ through Sb doping [6]. $BaSnO_3$'s band gap influenced by a splitting of energy levels was procured through Mn doping [7]. Improved crystalline quality through Au doping was quoted for $BaSnO_3$ by Athawale et al. [4]. Besides doping, reduced band gap is also possible by green synthesizing $BaSnO_3$ using plant leaf extracts which act as reducing, stabilizing, and capping agents [8]. A decreased band gap was reported for CeO_2/ZrO_2 core nanoparticles (NPs) biosynthesized using Justiciaadhatoda by Pandiyan et al. [9]. ZnO and NiO NPs green synthesized using M. Oleifera and neem leaves displayed reduced band gaps [10, 11].

Herein Moringa oleifera (M. oleifera) leaf extract is adapted to green synthesized $BaSnO_3$ NPs as it contains rich phytochemicals which reduce metal ions to nanoparticles in the chelating process. Various fatty acids, vitamins, amino acids and nutrients, glucosinolates, and phenolics such as flavonoids, anthocyanins, proanthocyanides, and micronutrients such as Cu, Mn, Fe, Co, and Ni are also present in M.oleifera extract [12]. In literature, silver and zinc oxide NPs for antibacterial application were green synthesized using M. oleifera by Irfan et al. [13]. M. oleifera

[Downloaded from basiji.iust.ac.ir on 2025-08-30]

[DOI: 10.22068/ijmse.2966]

mediated Ni-doped Fe_3O_4 exhibited excellent catalytic skill [14]. Super-paramagnetic behaviour was reported for iron oxide nanoparticles capped with M. Oleifera extract by Aisida et al. [15]. MgO [16] and TiO_2 [17] NPs were green synthesized using M. oleifera for antibacterial applications. To ascertain the dominance of phytochemicals of M. oleifera, in this work, $BaSnO_3$ was green synthesized using it, characterized, and compared with the results obtained for chemically synthesized $BaSnO_3$.

2. EXPERIMENTAL PROCEDURE

2.1. Materials

Barium chloride [$BaCl_2.2H_2O$] and tin(II) chloride [$SnCl_2.2H_2O$], both of analytical reagent (AR) grade obtained from Rankhem chemicals, India with 99.8% assay are the precursor salts used to synthesize $BaSnO_3$ NPs by chemical and greener methods.

2.2. Preparation of M. Oleifera Leaf Extract

Fresh M. Oleifera leaves were shade-dried and powdered after being cleaned with water. Then, 25 g of the powder was dissolved in a reaction mixture of ethanol (5 mL), and water (25 mL) and kept in soxhlet apparatus for two hours at 60°C. The resultant was filtered to get M. Oleifera leaf extract.

2.3. Chemical Synthesis of $BaSnO_3$ (CBS) NPs

Barium chloride and tin(II) chloride each of 0.1 M were dissolved in a reaction mixture containing de-ionized water (135 mL), dilute HCl (5 mL), and liquid ammonia (10 mL), stirred and aged for two hours. The settled precipitates were washed, dried, and calcined at 400°C for 1 h and crushed to form chemically synthesized $BaSnO_3$ designated as CBS.

2.4. Green Synthesis of $BaSnO_3$ (GBS) NPs

To green synthesize $BaSnO_3$, the precursor salts were dissolved in a reaction mixture containing 115 mL de-ionized water, 5 mL dilute HCl, and 30 mL leaf extract. By repeating the above procedure (Section 2.3), greener $BaSnO_3$ was synthesized, and designated as GBS. To avoid agglomeration, heat treatment was done at 200°C for 1 h [18].

2.5. Characterization

XRD, SEM, XPS, UV-Vis-NIR, FTIR, and PL details used to characterize the CBS and GBS samples are displayed in Table 1.

Table 1. Instruments used to characterize CBS and GBS NPs

Instrument	Model
XRD	PW 340/60 diffractometer
SEM	HITACHI S-3000H
FTIR	Perkin Elmer RX-1
UV-Vis	LAMBDA - 35
XPS	K-alpha™
PL	Varian Cary Eclipse spectrometer

2.6. Electrochemical Test

CV curves were acquired using scanning potentiostat/galvanostat (EG & G, model: 273 A) with a standard three-electrode configuration: CBS & GBS-Working electrode, conventional saturated calomel electrode (SCE)-Reference electrode and platinum-Counter electrode. 2 mg of the synthesized samples dissolved in ethylene glycol were brushed and coated on the surface on the glass substrates to use as working electrode.

2.7. NLO Studies

The third-order NLO studies were performed using a 532 nm diode-pumped CW Nd: YAG laser (coherent compass TM215 M–50), which was focused by a 3.5 cm focal length lens.

2.8. Catalytic Activity

The photocatalytic activity was evaluated by monitoring the deactivation of 0.05 M methyl violet dye under 60 W UV light irradiation. 10 mg of CBS and GBS NPs were added to a 100 mL aqueous solution containing the dye separately. Before light exposure, the dye solution with the catalysts was stirred to reach the absorption/ desorption equilibrium.

The degradation efficiency (η) and rate constant (k) were calculated using the dye concentrations in dark (C_0) and light (C) conditions:

$$\eta = \left(1 - {}^{C}/_{C_0}\right) \times 100\% \quad (1)$$

$$k = \frac{\ln(C_0/C)}{t} \quad (2)$$

2.9. Antibacterial Activity

Antibacterial activity was analyzed by well diffusion method against Proteus vulgaris bacteria. Proteus vulgaris strains were swapped in petriplates containing Mueller–Hinton agar medium in which 6 mg sample was placed in wells (6 mm diameter) and incubated for 24 h at

[Downloaded from basiji.iust.ac.ir on 2025-08-30]

[DOI: 10.22068/ijmse.2966]

37 ± 2°C. By measuring the inhibition zones, the bacterial suppression ability was evaluated.

2.10. In-vitro Cytotoxicity Activity

HepG2 human liver cancer cells were used for anticancer studies. Incubation at 37ºC was performed after seeding the cells in 10% Dulbeccos Modified Eagle Medium (DMEM) added to 96 well plates. At 80% confluence, the cells treated with different concentrations of the synthesized GBS NPs (10 µL, 20 µL, 30 µL, 40 µL, and 50 µL) were incubated for 24 h. After photographing, the cells were washed with 1xPBS and evaluated for cytotoxicity using MTT (Thiazolyl Blue Tetrazolium Bromide) and incubated for 4 hr in the dark, after which MTT was reduced into purple-colored formazan crystals which were mixed with dimethyl sulfoxide (DMSO) for complete solubility and absorbance spectra was taken at 570 nm.

3. RESULTS & DISCUSSION

3.1. XRD Studies

XRD patterns (Fig. 1(a, b)) indicate the cubic structural nature of both CBS and GBS NPs (JCPDS card No. 15-0780). Reduction in peak intensities and amorphous quality is noticed for the GBS sample due to bioactive active elements in the extract [12]. The crystallite sizes were 63 ± 2 nm and 49 ± 2 nm, respectively for the CBS and GBS samples.

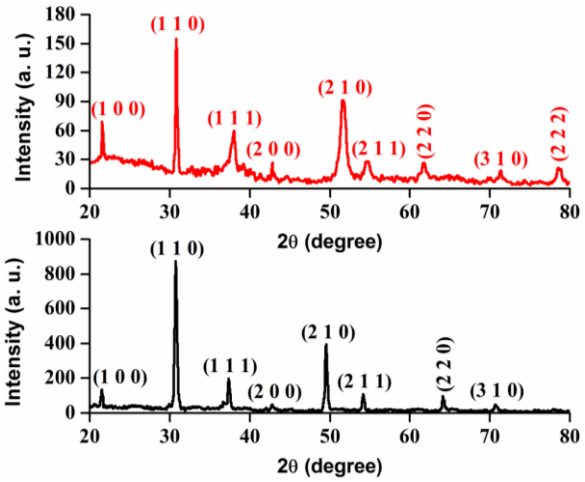

Fig. 1. XRD patterns of a) CBS and b) GBS NPs

3.2. SEM Analysis

The SEM images and histographs of a) CBS and b) GBS are pictured in Fig. 2 which showed grains with different sizes and shapes.

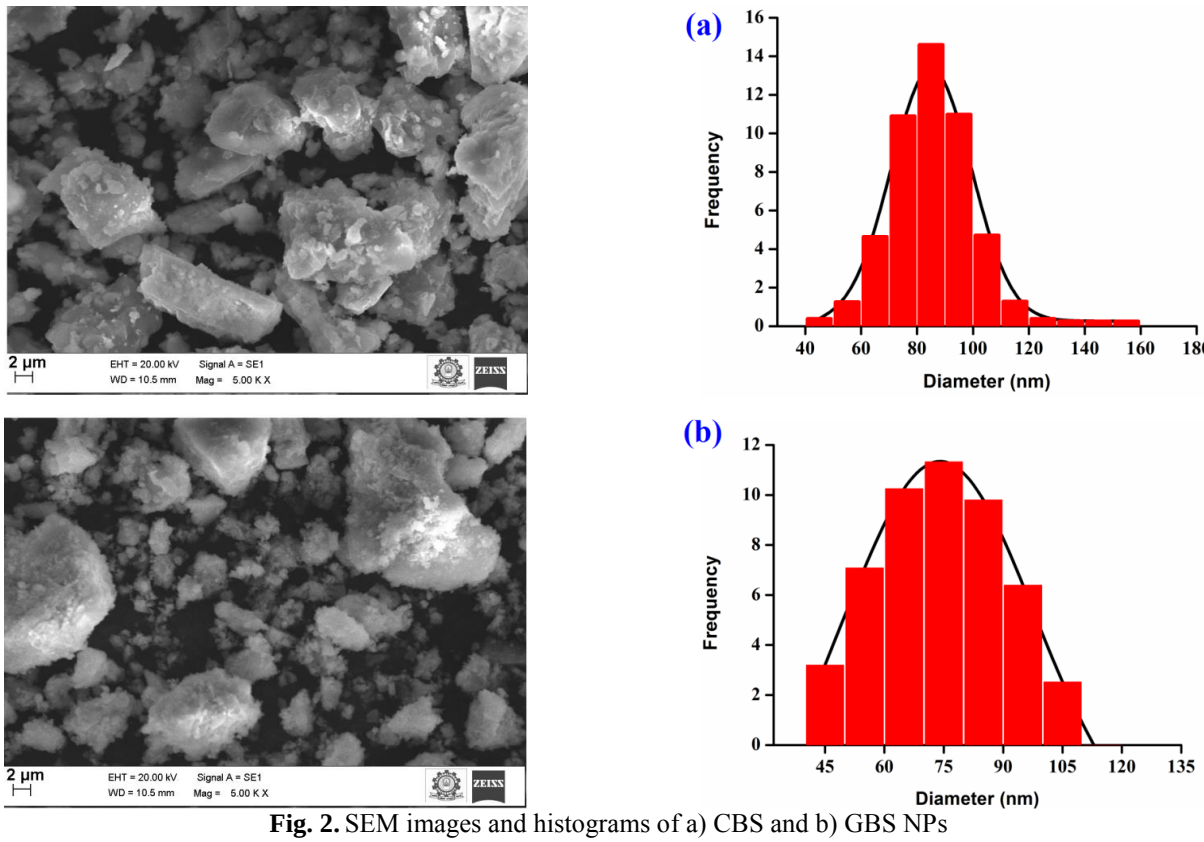

Fig. 2. SEM images and histograms of a) CBS and b) GBS NPs

[Downloaded from basiji.iust.ac.ir on 2025-08-30]

[DOI: 10.22068/ijmse.2966]

More agglomeration occurred for the GBS sample with many empty sites. The average grain sizes from the histograms were 84 ± 3 nm and 77 ± 3 nm, respectively for CBS and GBS which is consistent with the XRD results.

3.3. EDS and Mapping

Fig. 3 shows the EDS spectra of a) CBS and b) GBS nanoparticles, which affirmed the presence of Ba, Sn, and O. The atomic percentage compositions of the elements are displayed in the inset pie diagrams.

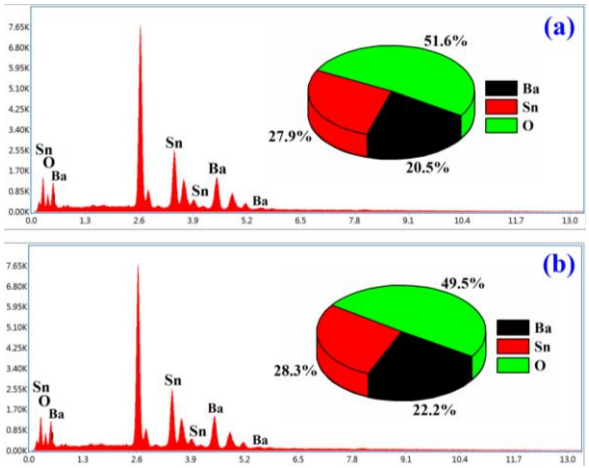

Fig. 3. EDX spectra of a) CBS and b) GBS NPs

Fig. 4 shows the mapping images of Ba, Sn, and O of a) CBS and b) GBS. The uniform distribution of elements slightly deviates for the greener sample owing to the capping of $BaSnO_3$ by the bioactive elements in the extract.

3.4. XPS Studies

The survey scan spectrum (Fig. 5 (a)) of GBS marks the residence of Ba, Sn, and O. The C1s signal located at 281.2 eV might have resulted from CO_2 absorbed [19]. The 792.8 and 777.8 eV peaks (Fig. 5(b)) assigned to Ba $3d_{3/2}$ and Ba $3d_{5/2}$ spin states coincide with Ba^{2+} [20]. The Sn $3d_{3/2}$ and $Sn3d_{5/2}$ peaks observed at 492.7 and 484.4 eV (Fig. 5(c)) correspond to Sn^{2+} in $BaSnO_3$ [21]. The core spectra for O1s (Fig. 5(d)) have a single peak at 529 eV attributed to O^{2-} ions in $BaSnO_3$ [22].

3.5. FTIR Studies

Fig. 6 shows the FTIR spectra of a) CBS and b) GBS samples. The OH stretching vibration-related peaks were observed between 3040 to 3860 cm^{-1} for both the samples [23], at 2808 cm^{-1} for CBS and 2812 cm^{-1} for GBS. The band at 1996 cm^{-1} corresponds to the S–O bending vibration [24]. The deformation mode of the OH group resulted in bands at 1751, 1636, and 1605 cm^{-1} for CBS and at 1755, 1611 cm^{-1} for GBS [25]. The 1402 cm^{-1} peak corresponds to C=O stretching [26]. C–O single bond stretching and OH bending mode vibrations are observed respectively at 1256 and 1032 cm^{-1} for GBS [27]. The SnO_6 stretching vibration peak at 679 cm^{-1} is connected to the barium ion [28]. The ν_{Sn-O} stretching appears at 565 cm^{-1} for CBS and at 561 cm^{-1} for GBS [4]. The metal-oxygen-related peak occurs at 415 cm^{-1} for the CBS sample.

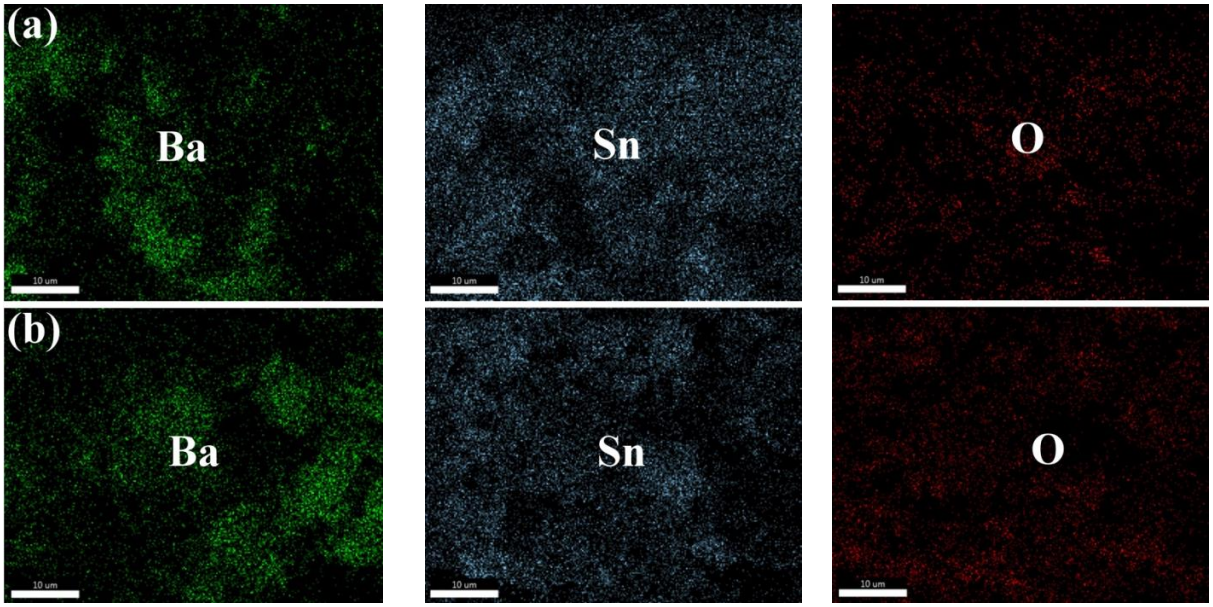

Fig. 4. Mapping images of Ba, Sn, and O of a) CBS and b) GBS NPs

[Downloaded from basiji.iust.ac.ir on 2025-08-30]

[DOI: 10.22068/ijmse.2966]

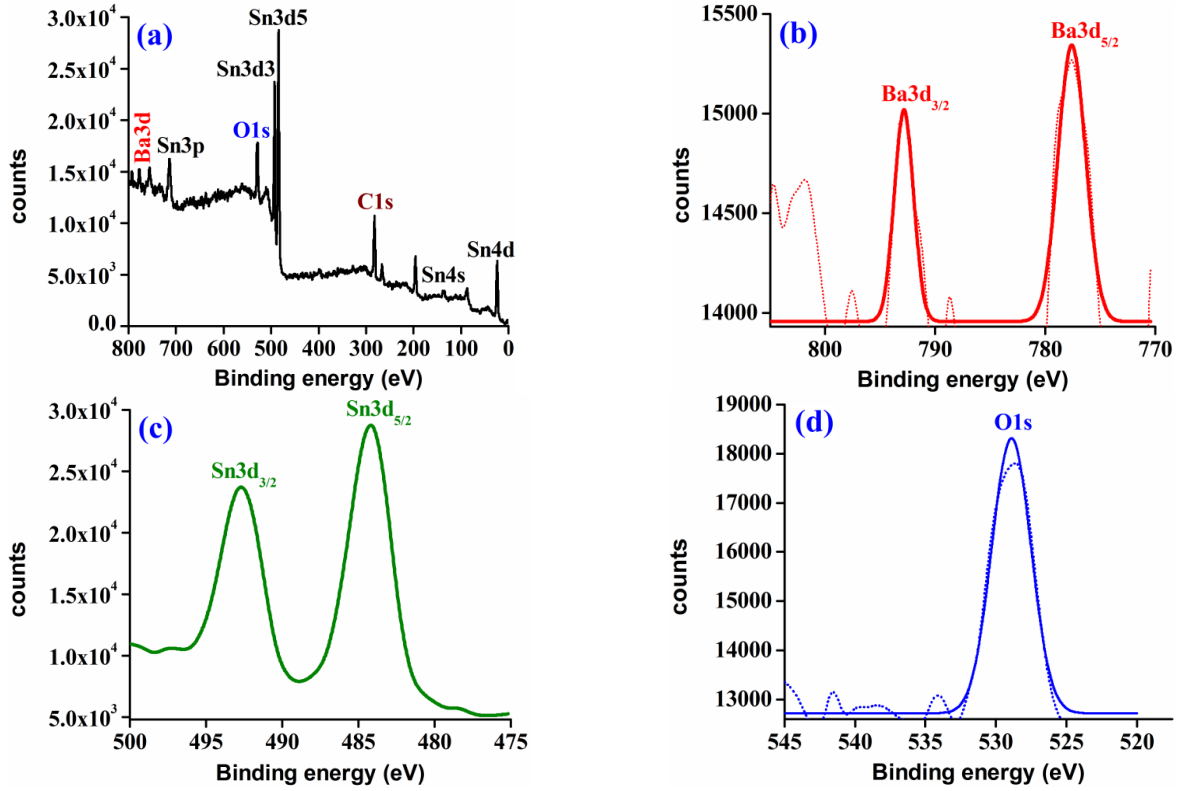

Fig. 5. a) Survey scan, core level spectra of b) Ba, c) Sn, and d) O of the greener $BaSnO_3$

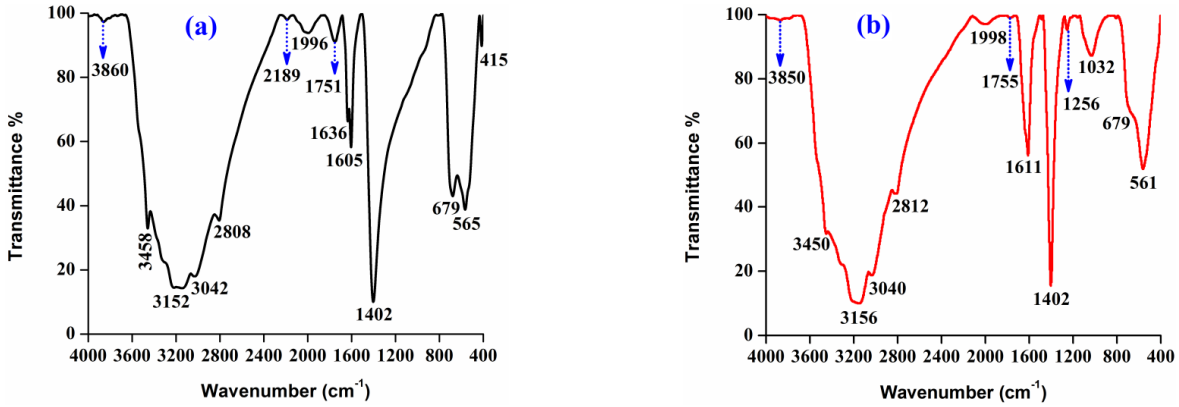

Fig. 6. FTIR spectra of a) CBS and b) GBS NPs

3.6. DRS Studies

Fig. 7 shows the transmittance spectra of a) CBS and b) GBS NPs. Even though high transparency occurs for the greener sample in the 900–1400 nm region, a remarkable drop is experienced in the 400–900 nm range due to increased absorption (Inset Fig). For the greener $BaSnO_3$, strong surface plasmon resonance peaks occur at 420 and 640 nm in the wavelength region 300–700 nm, which highlighted that M. oleifera extract has dominated its optical absorption ability and agrees with earlier reports [29, 30]. The energy gap values of the CBS and GBS samples were estimated by calculating the Kubelka–Munk function (K_M) from the diffuse reflectance (R) values using the relation [31]:

$$K_M = \frac{(1-R)^2}{2R} \quad (3)$$

Using the K_M values, plots were drawn between $(K_M h\nu)^2$ vs $h\nu$ (Fig. 8) and the band gap (E_g) values were calculated to be 3.23 ± 0.01 eV and 3.04 ± 0.01 eV, respectively for CBS and GBS NPs. The obtained band gap value for the CBS sample agrees with the value reported earlier [1]. The reduced E_g value for the GBS sample is due to phytochemicals in the leaf extract which acts as

[Downloaded from basiji.iust.ac.ir on 2025-08-30]

[DOI: 10.22068/ijmse.2966]

a reducing agent [32].

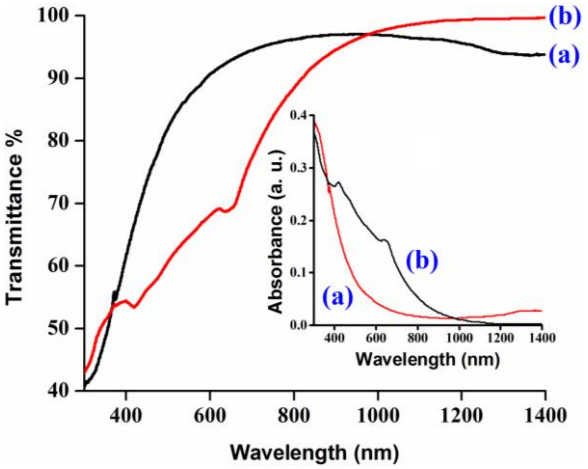

Fig. 7. Transmittance and absorption spectra of a) CBS and b) GBS NPs

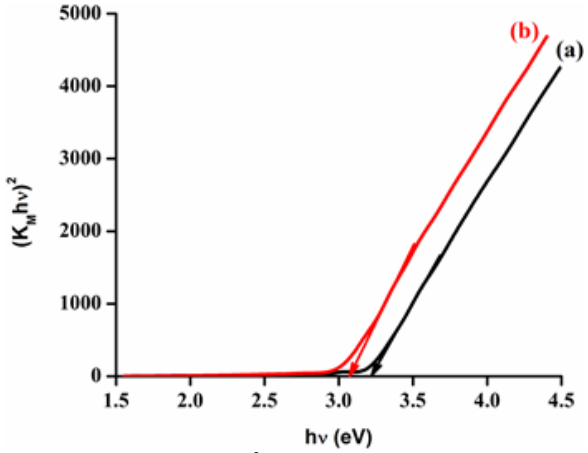

Fig. 8. Plots of $[K_M h\nu]^2$ vs. hν of a) CBS and b) GBS NPs

3.7. PL Studies

In the PL spectra (Fig. 9(a, b)) emission peaks were observed at 361, 380, 412, and 490 nm for both the samples. Radiative recombination of free excitons emits the NBE ultra-violet emission at 361 and 380 nm, respectively [33]. Oxygen vacancies correspond to the 412 nm band for both the samples and at 437 nm for the greener sample [34]. The size-dependent excitonic transition peak is seen at 490 nm [35]. The decreased PL intensities realized for the GBS sample might be responsible for its enhanced photogenerated electron-hole pair separation which enhances its bacterial suppression (Section 3.11). The decreased intensity might be attributed to the decreased crystallite size due to the increased number of defects [36]. A decrease in crystallite size increases non-radiative oxygen vacancies and photoexcited electrons are trapped within those vacancies, thereby decreasing their recombination with holes [37].

3.8. Electrochemical Studies

Fig. 10 shows the cyclic voltammetric curves of CBS and GBS NPs. The CV curves reveal two distinct redox couples (oxidation and reduction process) supporting pseudocapacitive behaviour [38]. Increased peak area with increased peak current realized for the greener $BaSnO_3$ confirmed its superior electrochemical behaviour. The specific capacitance (C_S) values calculated by the relation, $C_S = \frac{I\Delta t}{m\Delta V}$ are 29 ± 0.05 and 46 ± 0.05 F/g, respectively for the chemical and greener $BaSnO_3$. The higher C_S value obtained for the greener sample favours its improved electrochemical behaviour [39]. To understand the interfacial charge transfer process between the electrode and electrolyte, EIS measurements were performed and shown in Fig. 11.

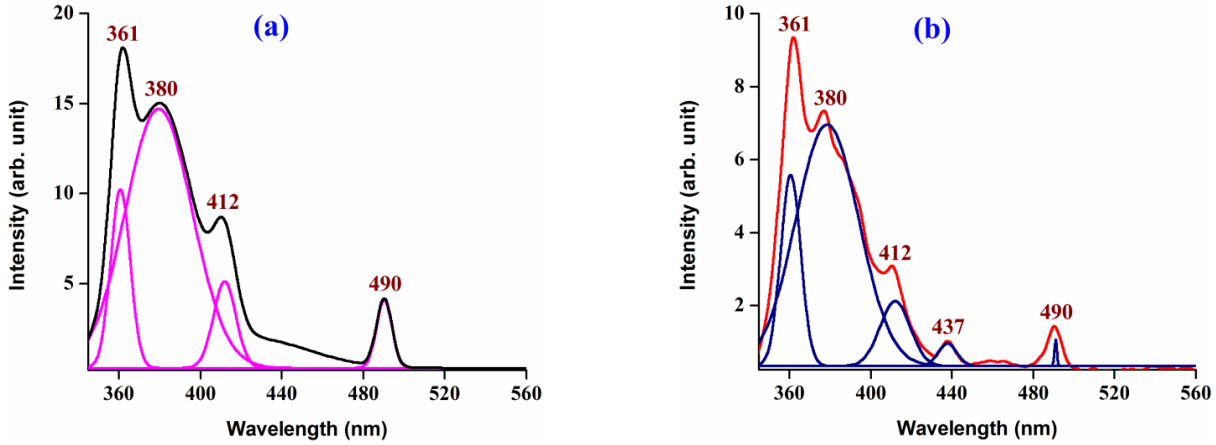

Fig. 9. PL spectra of CBS and GBS NPs

[Downloaded from basiji.iust.ac.ir on 2025-08-30]

[DOI: 10.22068/ijmse.2966]

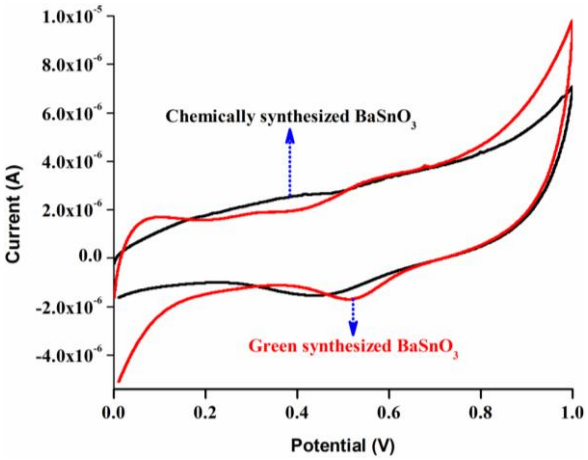

Fig. 10. CV curves of CBS and GBS NPs

In the high-frequency domain, both CBS and GBS samples demonstrate a semicircular pattern and in the low-frequency domain they reveal a linear segment [40]. The decreased diameter observed for the GBS sample promotes reduced polarization and low charge transfer resistance which facilitates accelerated ion diffusion in the electrolyte. The R_{ct} values were 5330 and 3185 ohms for the CBS and GBS samples, respectively. The GBS sample's potential as a supercapacitor was validated by its lowest charge transfer resistance value.

3.9. Z-scan Studies

Fig. 12 shows the Z-scan (a) closed, (b) open, and (c) closed-to-open aperture curves of CBS and GBS nanoparticles. Pre-focal peak along with the post-focal valley in the closed-aperture curve indicates negative non-linearity revealing that the nonlinear refraction is positive due to the thermo-optic or thermal defocusing effect [41].

The nonlinear refractive index n_2 values are 5.24 x 10^{-9} cm^2/W and 6.16 x 10^{-9} cm^2/W respectively for the CBS and GBS NPs. The open aperture curves confirmed that both the samples display a reverse saturation absorption (RSA) process by stout nonlinear absorption at the origin (Z= 0) which occurs either from single photon absorption or multi-photon absorption [42]. The nonlinear absorption coefficient (β) values of the CBS and GBS NPs are 3.26 x 10^{-4} cm/W and 3.26 x 10^{-4} cm/W, respectively.

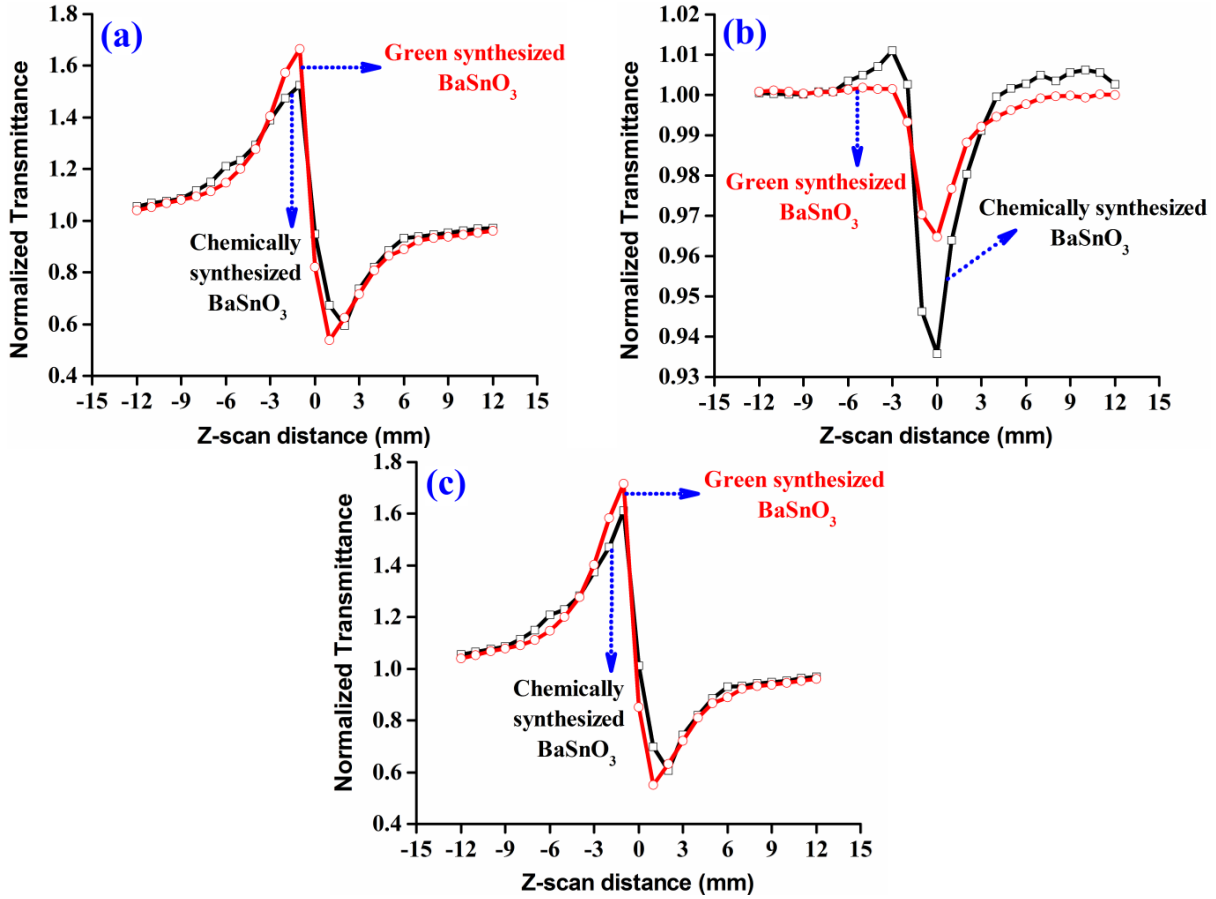

Fig. 11. Nyquist plots of CBS and GBS

[Downloaded from basiji.iust.ac.ir on 2025-08-30]

[DOI: 10.22068/ijmse.2966]

The third-order nonlinear optical susceptibility values are compiled in Table 2. The GBS sample possesses high third-order NLO susceptibility due to more electron cloud movement from the donor to the acceptor confirming its utility for photonic applications.

3.10. Photocatalytic Test

Methyl violet was tested under UV light to justify the dye-deactivation ability of CBS and GBS catalysts. Fig. 13 shows the absorption spectra of the catalysts measured at 587 nm. For both catalysts, absorbance decreased with an increase in irradiation time, confirming their degrading nature. The degradation efficiencies were calculated using Eqn. (1) is compiled in Table 3.

The maximum degradation efficiencies achieved for CBS and GBS catalysts after 90 min light irradiation were 78.4% and 89.7%, respectively. The photoefficiency depends on the charge transfer, electron-hole recombination, and light absorption properties. When light falls on CBS and GBS catalysts (Fig. 14), electrons in their valence bands are excited and move to their conduction bands; leaving holes in VB. The electrons react with surrounding oxygen and reduce to O_2^{*-}; whereas holes left in the VB oxidize OH^- derived from adsorbed water to form OH^*. The O_2^{*-} and OH^* radicals have a strong oxidative ability and decompose MV dye into CO_2, H_2O, and small molecules [43]. The increased degradation efficiency observed for the GBS catalyst might be due to the easy excitation of phytochemicals present in the leaf extract which are loaded on $BaSnO_3$ which creates more mobile electrons and hence more O_2^{*-} radicals are produced [44]. Also, the photo-excited electrons of the phytochemicals are easily transferred to the conduction band of GBS which creates more active sites, which enhances the electron-hole separation thereby improving the degradation efficiency [45]. The apparent rate constants (k) estimated from the slopes of the plots of $\ln(C_0/c)$ vs. irradiation time was 0.01907 min^{-1} and 0.02685 min^{-1} for CBS and GBS, respectively. The higher value of k obtained for the GBS sample favours its higher degradation efficiency.

Table 2. Third order nonlinear optical susceptibility values of CBS and GBS NPs

Sample	Optical susceptibility		
	Real part (R_e) $\chi^{(3)}$ x 10^{-6} esu	Imaginary part (I_m) $\chi^{(3)}$ x 10^{-6} esu	Absolute value χ^3 x 10^{-6} esu
CBS	5.48	2.12	5.87
GBS	6.03	2.27	6.45

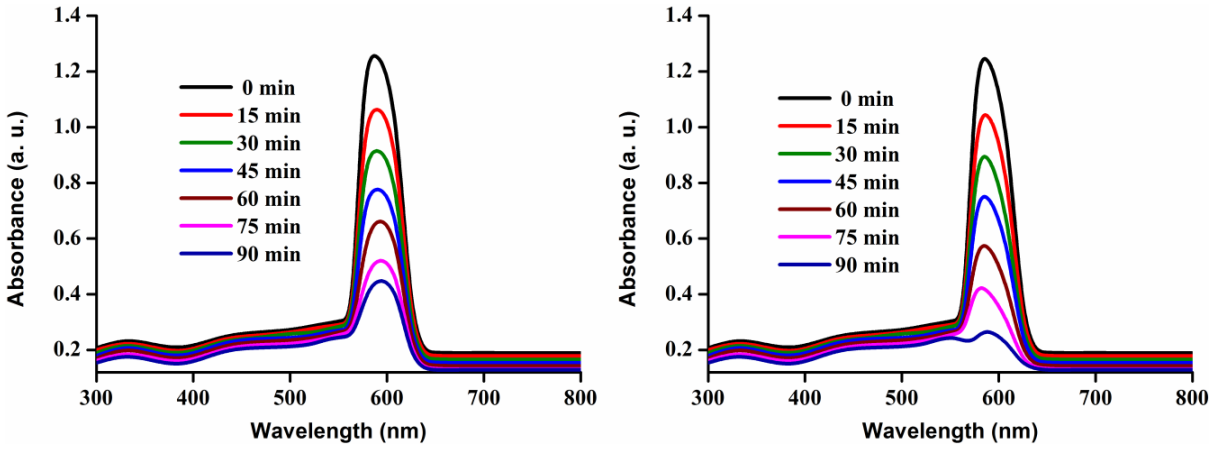

Fig. 12. Z-scan a) closed aperture b) open aperture and c) closed-to-open aperture curves of CBS and GBS NPs

Table 3. Photodegradation efficiencies of CBS and GBS catalysts

Sample	Photodegradation efficiency (%)					
	Irradiation time (min)					
	15	30	45	60	75	90
CBS	9.5	20.3	37.8	52.7	68.4	78.4
GBS	19.1	36.8	52.9	69.1	79.4	89.7

[Downloaded from basiji.iust.ac.ir on 2025-08-30]

[DOI: 10.22068/ijmse.2966]

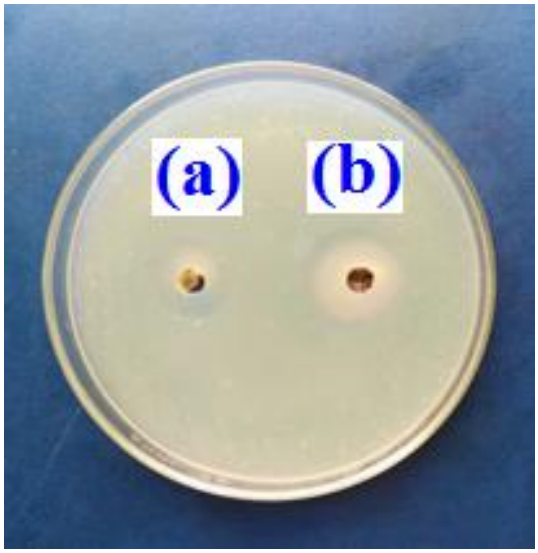

Fig. 13. Absorption spectra for a) CBS and b) GBS catalysts against MV dye

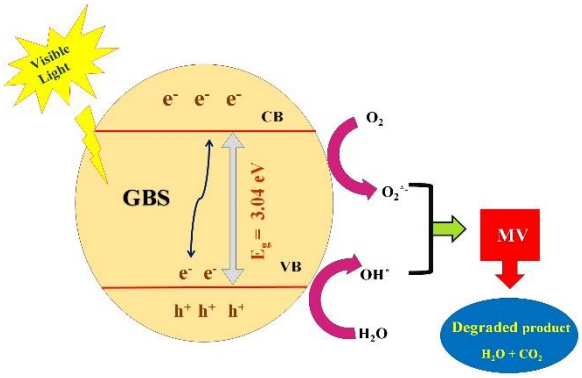

Fig. 14. Photocatalytic mechanism involved with GBS catalyst

3.11. Bacterial Suppression

The antibacterial activity of the CBS and GBS samples is shown in Fig. 15 (a, b). The greener sample showed higher antibacterial activity (Fig. 15(b)) against the tested bacteria. The bacterial suppression of the CBS and GBS NPs relies on their contact with the bacterial membrane which collapses and ruptures it thereby leaking bacterial cytoplasm [46]. When the bacterial cells and NPs interact, reactive oxygen species (ROS) are generated which tear down the bacterial membrane [47]. ROS generation inhibits protein synthesis, DNA replication, and the metabolism cycle damaging the bacterial cell [48]. Also, the release of constituent metal ions from the surface contributes to the antibacterial activity. These ions which are in direct contact with the bacteria are absorbed by its outer membrane. They react with this membrane according to the electronegative tendencies of the element which creates a hole in the bacterial membrane, ultimately leading to its demise [49]. More ROS are generated for the greener sample due to decreased crystallite size which makes it more effective in resisting bacterial growth. Also, the hydroxyl group-related phenols in the extract exhibit better scavenging ability and hence enhanced bacterial suppression was realized for the greener $BaSnO_3$.

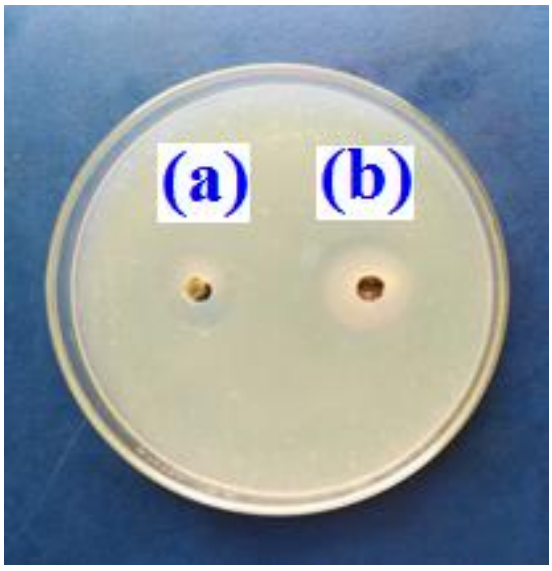

Fig. 15. Bacterial suppression of a) CBS and b) GBS NPs against Proteus vulgaris bacteria

3.12. Anticancer Activity

The extract-mediated $BaSnO_3$ effectively resisted the tested HepG2 cancer cells; on the other hand, the control and the chemically synthesized $BaSnO_3$ showed no sign of resistance (Fig. 16(a-e)). From the graph between cell viability and the concentration of the sample (Fig. 17), the sample with 40 µL concentration exhibited better cytotoxicity against the tested cells. The effective cytotoxicity realized for the extract-mediated sample might be due to smaller crystallite size, larger surface area, electrostatic fascination between +vely charged GBS NPs and –vely charged cells which demise the HepG2 cell by membrane leakage, ROS generation, and induction of apoptosis which cause the death of the cells. Eicosane in an appreciable quantity in the leaf extract might have dominated the anticancer ability of the green synthesized $BaSnO_3$.

[Downloaded from basiji.iust.ac.ir on 2025-08-30]

[DOI: 10.22068/ijmse.2966]

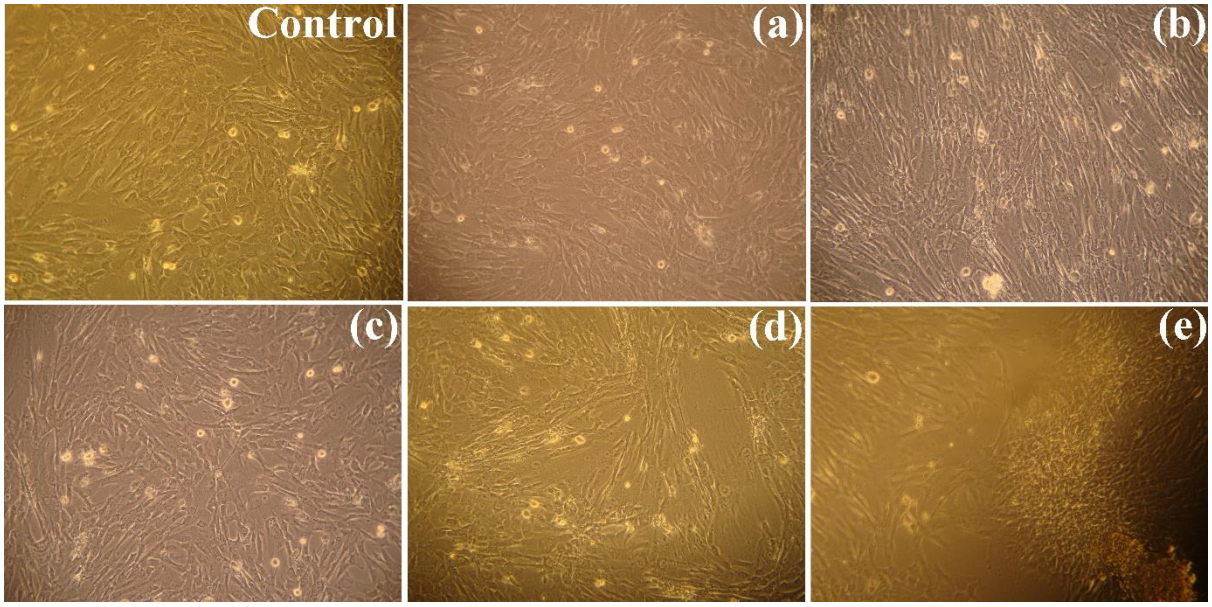

Fig. 16. Anticancer activity of the green synthesized CuS NPs with a) 10 µL, b) µL, c) 30 µL, d) 40 µL and e) 50 µL concentrations

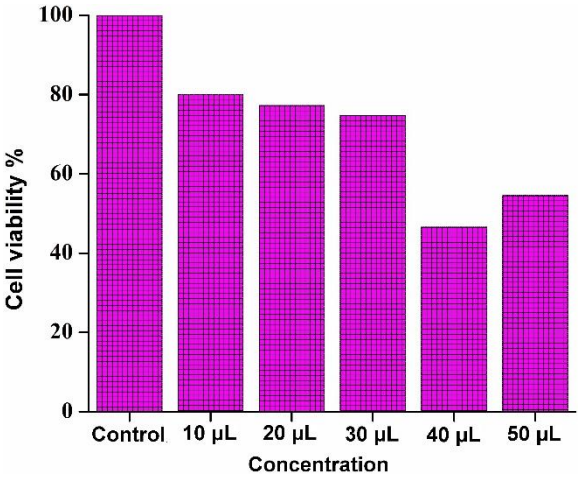

Fig. 17. Variation of cell viability with the concentration of the CuS NPs

4. CONCLUSION

Comparison of the electrochemical, nonlinear optical, catalytic, antimicrobial, and anticancer properties of chemical and green synthesized $BaSnO_3$ perovskite. Decreased crystallite size and increased specific capacitance were achieved for the greener $BaSnO_3$. The greener $BaSnO_3$ exhibited remarkable third-order NLO properties and it degraded 89.7% of methyl violet dye within 90 min under UV light irradiation. Excellent bacterial suppression and anticancer activity were observed for the greener sample. The obtained results endorsed that the M. oleifera leaf extract mediated greener $BaSnO_3$ perovskite which was synthesized without employing toxic solvents was facile, green, and suitable for large area production to be used as efficient electrode materials in pseudo capacitors, optical switching, catalytic and biomedical applications.

ACKNOWLEDGEMENTS

Kalasalingam University, India is very much thanked for the mapping images.

REFERENCES

[1]. James, K. K., Aravind, A., and Jayaraj, M. K., "Structural, Optical and Magnetic Properties of Fe-Doped Barium Stannate Thin Films Grown by PLD." Appl. Surf. Sci., 2013, 282, 121-125.

[2]. Kozlovskiy, A, Kenzhina, I., and Zdorovets, M., "Synthesis, Bhase Composition and Magnetic Properties of Double Perovskites of A (FeM)O4-x type (A=Ce, M=Ti)." Ceram. Int., 2019, 45, 8669-8676.

[3]. Hadjarab, B., Bouguelia, A., and Trari, M., "Synthesis, Physical and Photo Electrochemical Characterization of La-doped $SrSnO_3$." J. Phys. Chem. Solids, 2007, 68, 1491-1499.

[4]. Athawale, A. A., Bapat, M. S., and Desai, P. A., "Hydrothermal Preparation of $BaSnO_3$ and Au-$BaSnO_3$ Nanorods." J. Nanosci. Nanotechnol., 2008, 8, 4258-

[Downloaded from basiji.iust.ac.ir on 2025-08-30]

[DOI: 10.22068/ijmse.2966]

4262.

[5]. John, J, Mahadevan Pillai,V. P., Thomas, A. R., Philip, R., Joseph, J., Muthunatesan, S., Ragavendran, V., and Prabhu, R., "Synthesis, Structural and Morphological Property of $BaSnO_3$ Nanopowder Prepared by Solid State Ceramic Method." IOP. Conf. Series, 195, 2017, 012007.

[6]. Liu, Q., Dai, J., Liu, Z., Zhang, X., Zhu, G., and Ding, G., "Electrical and Optical Properties of Sb-doped $BaSnO_3$ Epitaxial Films Grown by Pulsed Laser Deposition." J. Phys. D: Appl. Phys., 43, 2010, 455401.

[7]. Balamurugan, K., Kumar, N.H., Ramachandran, B., Rao, M.S.R., Chelvane, J.A., and Santhosh, P.N., "Magnetic and Optical Properties of Mn-doped $BaSnO_3$". Sol. State Commun., 2009, 149, 884-887.

[8]. Darvishi, E., Kahrizi, D., and Arkan, E., "Comparison of Different Properties of Zinc Oxide Nanoparticles Synthesized by the Green (using Juglans regia L. leaf extract) and Chemical methods." J. Mol. Liq., 2019, 286, 110831.

[9]. Pandiyan, N., Murugesan, B., Sonamuthu, J., Samayanam, S., and Mahalingam, S., "Facile Biological Synthetic Strategy to Morphologically Aligned CeO_2/ZrO_2 Core Nanoparticles using Justice Adathoda Extract and Ionic Liquid: Enhancement of its Bio-Medical Properties." J. Photochem. Photobiol. B. Biol., 2018, 178, 481-488.

[10]. Matinise, N., Fuku, X. G., Kaviyarasu, K., Mayedwa, N., and Maaza, M., "ZnO Nanoparticles via Moringa oleifera Green Synthesis: Physical Properties & Mechanism of Formation." Appl. Surf. Sci., 2017, 406, 339-347.

[11]. Helan, V., Joseph Prince, J., Al-Dhabi, N. A., Arasu, M. V., Ayeshamariam, A., Madhumitha, G., Roopan, S. M., and Jayachandran, M., "Neem Leaves Mediated Preparation of NiO Nanoparticles and its Magnetization, Coercivity, and Antibacterial Analysis. Res. Phys., 2016, 6, 712-718.

[12]. Kayathiri, C., Balu, A. R., Suganya, M., Vinitha, G., Delci, Z., Balamurugan, S., Karthika, M., Anitha, S., and Prabavathi, A., "$BaZrO_3$ Perovskite–A UV Light Mediated Congo Red Dye Deactivator Catalyst Good Optical Switching and Antimicrobial Abilities Green Synthesized using Moringa oleifera Leaf Extract". Mater. Sci. Eng. B, 2022, 278, 115636.

[13]. Irfan, M., Munir, H., and Ismail, H., "Moringa oleifera Gum Based Silver and Zinc Oxide Nanoparticles: Green Synthesis, Characterization and their Antibacterial Potential Against MRSA." Biomater. Res. 2021, 25, 17.

[14]. Prasad, C., Sreenivasulu, K, S., Gangadhara, K., and Venkateswarlu, P., "Bio Inspired Green Synthesis of Ni/Fe_3O_4 Magnetic Nanoparticles Using Moringa oleifera Leaves Extract: A Magnetically Recoverable Catalyst for Organic Dye Degradation in Aqueous Solution." J. Alloys. Compnd., 2017, 700, 252-258.

[15]. Aisida, S. O., Ugwu, K., Akpa, P. A., Nwanya, A. C., Nwankwo, U., Bashir, A. K. H., Madiba, I. G., Ahmed, I., and Ezema, F. I., "Synthesis and Characterization of Iron Oxide Nanoparticles Capped with Moringa oleifera: The Mechanisms of Formation Effects on the Optical, Structural, Magnetic and Morphological Properties." Mater. Today Proc., 2021, 36, 214-218.

[16]. Amrulloh, H., Fatiqin, A., Simanjuntak, W., Afriyani, H., and Annissa, A., "Antioxidant and Antibacterial Activities of Magnesium Oxide Nanoparticles Prepared Using Aqueous Extract of Moringa oleifera Bark as Green Agents." J. Multidisciplinary Appl. Nat. Sci., 2021, 1, 44-53.

[17]. Patidar, V., and Jain, P., "Green Synthesis of TiO_2 Nanoparticles Using Moringa oleifera Leaf Extract", Int. Res. J. Eng. Technol., 2017, 4, 470 -473.

[18]. Suganya, M., Balu, A. R., Anitha, S., Prabha, D., Balamurugan, S., Priyanka, B., and Nagarethinam, V. S., "PbS-NiO Nanocomposite Material with Enhanced Magnetic, Photocatalytic and Antifungal Properties." Mater. Sci. Eng. B, 2018, 229, 118 -125.

[19]. Zhou, Y., Xu, L., Wu, Z., Li, P., and He, J., "Optical and Photocatalytic Properties of Panocrystalline ZnO Powders Synthesized by a Low Temperature Hydrothermal Method." Optik, 2017, 130, 673-680.

[20]. Chakrabarti, S., Ginnaram, S., Jana, S., Wu, Z. Y., Singh, K., Roy, A., Kumar, P., Maikap, S., Qiu, J. T., Cheng, H. M., Tsai,

[Downloaded from basiji.iust.ac.ir on 2025-08-30]

[DOI: 10.22068/ijmse.2966]

L. N., Chang, Y., Lu., Mahaputra, R., and Yang, J. R., "Nagativecoltage Modulated Multi-level Resistive Switching by Using a Cr/BaTiOx/TiN Structure and Quantum Conductance through Evidence of H_2O_2 Sensing Mechanism". Sci. Rep., 2017, 7, 1-13.

[21]. Nallendran, R., Selvan, G., and Balu, A. R., "Photocatalytic Performance of SnO_2 Coupled CdO Nanoparticles Against MY and RhB Dyes". J. Electron. Mater., 2019, 46, 3676-3685.

[22]. Prasad, A. R., Garvasis, J., Oruvil, S. K., and Joseph, A., "Bio-inspired Green Synthesis of Zinc Oxide Nanoparticles Using Abelmoschus Eculentus Mucilage and Selective Degradation of Cationic Dye Pollutanta". J. Phys. Chem. Sol., 2019, 127, 265-274.

[23]. Balamurugan, S., Balu, A. R., Usharani, K., Narasimman, V., Suganya, M., and Nagarathinam, V. S., "CdO-Al_2O_3- A Composite Material with Enhanced Photocatalytic Activity Against the Degradation of MY Dye". Vacuum, 2019, 159, 9-16.

[24]. Srivind, J., Nagarethinam, V. S., Balamurugan, S., Anitha, S., Suganya, M., Praba, D., and Balu, A. R., "Synthesis and Characterization of Zr-doped SnS_2 Nanopowders by a Simple Soft Chemical Route towards Magnetic and Antibacterial Applications". Surf. Interfaces, 2017, 9, 58-63.

[25]. Nasir, Z., Shakir, M., Wahab, R., Shoeb, M., Alam, P., Khan, R. H., Mobin, M., and Lutfullah., "Co-precipitation Synthesis and Characterization of Co doped SnO_2 NPs, HSA Interactionvia Various Spectroscopic Techniques and their Antimicrobial and Photocatalytic Activities". Int. J. Bio. Macromol., 2017, 94, 554-565.

[26]. Raja, N., Nagarethinam, V. S., Manjula, N., Rajashree, C., Suganya, M., Balamurugan, S., Usharani, K., and Balu, A. R., "Structural, Optical, Electrical and Catalytic Properties of Precursor-Solution Aged Spray Deposited Undoped, Zn-doped and Ag-doped CdO Thin Films". Bull. Mater. Sci., 2020, 43, 117.

[27]. Subban, Md. A., Ahmed, T., Uddin, N., Azad, A.K., and Begum, K., "Synthesis, Characterization, PL Properties, Photocatalytic and Antibacterial Activities of Nano Multi-Metal Oxide NiO. CeO_2 .ZnO". Spact. Acta Part A. Mol. Biomol. Spect., 2014, 136, 824-831.

[28]. Anasree, Md. J., Kumar, U., and Upadhyay, S., "Solid-State Synthesis of Nanosized $Ba(Ti_{1-x}Sn_x)O_3$ Powders and Dielectric Properties of Corresponding Ceramics". Appl.Phys. A, 2017, 123, 1-12.

[29]. Akintelu, S. A., Folorunso, A. S., Folorunso, F. A., and Oyebamiji, A. K., "Green Synthesis of Copper Oxide Nanoparticles for Biomedical Application and Environmental Remediation". Heliyon, 2020, 6, 004508.

[30]. Jamdagni, P., Khatri, P., and Rana, J. S., "Green Synthesis of Zinc Oxide Nanoparticles Using Flower Extract of Nyctanthesarbor-tristis and their Antifungal Activity". J. King. Saud. Univ. Sci., 2016, 30, 168-175.

[31]. Nallendran, R., Selvan, G., and Balu, A. R., "Photoconductive and Photoconductive Properties of CdO-NiO Nanocomposite Synthesized by a Cost Effective Chemical Method". J. Matter. Sci. Mater. Electron., 2018, 29, 11384-11393.

[32]. Fu, L., and Fu, Z., "Plectranthus Amboinicus Leaf Extract Assisted Biosynthesis of ZnO Nanoparticles and their Photocatalytic Activity". Ceram. Int., 2015, 41, 2492-2496.

[33]. Sci, Y. R., Cao, Y., Li, X. F., Yue, Y. G., Yao, B., Li, X. Y., Lang, J. H., and Yang, J. H., "Structural and Optical Analysis of Zn1-xCdx O Nanopowder Synthesized by Hydrothermal Method". Ceram. Int., 2014, 41, 587-593.

[34]. Gu, F., Wang, S. F., Lu, M. K., Zhou, G. J., Xu, D., and Yuan, D. R., "Photoluminescence Properties of SnO_2 Nanoparticles Synthesized by Sol-gel Method". J. Phys. Chem. B, 2004, 108, 8119-8123.

[35]. Balamurugan, S., Balu, A. R., Narasimman, V., Selvan, G., Usharani, K., Suganya, M., Manjula, N., Rajeshree, C., and Nagarethinam, V. S., "Multi Metal Oxide CdO-Al_2O_3-NiO Nanocomposite-Synthesis, Photocatalytic and Magnetic Properties". Mater. Res. Exp., 2019, 6,

[Downloaded from basiji.iust.ac.ir on 2025-08-30]

[DOI: 10.22068/ijmse.2966]

015022-015031.
[36]. Nithya, N., Bhoopathi, G., Magesh, G., and Daniel Nesa Kumar, C., "Neodymium Doped TiO_2 Nanoparticles by Sol-gel Method for Antibacterial and Photocatalytic Activity". Mater. Sci. Semicond. Proc., 2018, 83, 70-82.
[37]. Anitha, V. S., Sujatha Lekshmy, S., and Joy, K., "Effect of Mn Doping on the Structural, Magnetic, Optical and Electrical Properties of ZrO_2–SnO_2 Thin Films Prepared by Sol–gel Method". J. Alloys. Compnd., 2016, 675, 331-340.
[38]. Bharathy, G., and Raji, P., "Pseudocapacitance of Co Doped NiO Nanoparticles and its Room Temperature Ferromagnetic Behaviour". Phys. B Conden. Matter, 2018, 530, 75-81.
[39]. Qashqay, S.M., Rahimi, J., Zamani-Meymian, M.R., and Maleki, A., "Porous Co_3O_4/VS4/rGO-SDBS@NF nanoflower as a high performance supercapacitor electrode." J. Energy Storage., 2023, 72, 108548.
[40]. Qashqay, S.M., Zamani-Meymian, M., Maleki, A., and Lahrami, Z.Z., "Fabrication of an asymmetric supercapacitor using a novel electrode design and introduce a robust machine learning model for its performance evaluation." J. Power Sources, 2024, 613, 234911.
[41]. Zongo, S., Sanusi, K., Britton, J., Mthunzi, P., Nyokong, T., Maaza, M., and Sahraoui, B., "Non-Linear Optical Properties of Natural Laccaic Acid Dye Studied using Z-Scan Technique". Optical Mater., 2015, 46, 270-275.
[42]. Ramya, E., Veeramohan Rao, M., and Narayana Rao, D., "Nonlinear Optical Properties of Ag- Enriched ZnO Nanostructures". J. Nonlinear, Opt. Phys. Mater., 2019, 28, 1950027-1950036.
[43]. Jang, Y. J., Simer, C., and Ohm, T., "Comparison of Zinc Oxide Nanoparticles and its Nanocrystalline Particles on the Photocatalytic Degradation of Methylene Blue". Mater. Res. Bull., 2006, 41, 67-77.
[44]. Amanulla, M., Shahina, A. J., Sundaram, S. K., Magdalane, R. M., Kaviyarasu, C., Letsholathebe, K. D., Mohamed, S. B., Kennedy, J., and Maaza, M., "Antibacterial, Magnetic, Optical and Humidity Sensor Studies of β- $CoMoO_4$-Co_3O_4 Nanocomposites and its Synthesis and Characterization". J. Photochem. Photobiol. B. Biol., 2018, 183, 233-241.
[45]. Perillo, P. M., and Atia, M. N., "Solar-assisted Photodegradation of Methyl Orange Using Cu-Doped ZnO Nanorods". Mater. Today Commun., 2018, 17, 252-258.
[46]. Ogunyemi, S. O., Addallah, Y., Zhang, M., Fouad, H., Hong, X., Ibrahim, E., Mahidul, Md., Masum, I., Hossain, A., Mo, J., and Li, B., "Green synthesis of Zinc Oxide Nanoparticles Using Different Plant Extracts and their Antibacterial Activity Against Xanthomonas oryzaepv. Oryzae". Artificial cells Nanomed. Biotechnol., 2019, 47, 341-352.
[47]. Xia, T., Kovochich, M., Brant, J., Hotze, M., Sempt, J., Oberley, T., Sioutas, C., Yeh, J. I., Weisner, M. R., and Nel, A. E., "Comparison of the Abilities of Ambient and Manufactured Nanoparticles to Induce Cellular Toxicity According to an Oxidative Stress Paradigm". Nano. Lett., 2006, 6, 1794-1807.
[48]. Buzea, C., Pacheco, I., and Robbie, K., "Nanomaterials and Nanoparticles: Sources and Toxicity". Biointerphases, 2007, 2, MR17 – 71.
[49]. Qashqay, S.M., Zamani-Meymian, M., and Sadati, S.J, "Improving antibacterial ability of Ti-Cu thin films with co-sputtering method." Sci. Rep, 2023, 13, 16593.

[Downloaded from basiji.iust.ac.ir on 2025-08-30]

[DOI: 10.22068/ijmse.2966]